AIAA JOURNAL
Vol. 36, No. 8, August 1998

Suppression of Flame Wrinkling by Buoyancy: The Baroclinic Stabilization Mechanism

Jose O. Sinibaldi,* Charles J. Mueller,† Alan E. Tulkki,‡ and James F. Driscoll§
University of Michigan, Ann Arbor, Michigan 48109

Buoyancy forces are known to alter the burning velocity of a turbulent flame by modifying the flame wrinkling process. To quantify how flame wrinkles are amplified or attenuated by buoyancy, a repeatable wrinkle of known size and amplitude is created in a premixed flame by interacting the flame with a vortex. Images of the wrinkle amplitude were obtained for microgravity conditions in the NASA Lewis Research Center 2.2-s drop tower and for 1-*g* conditions. Both thermodiffusively stable and unstable cases were considered. Results quantify the degree to which buoyancy suppresses the flame wrinkling; when buoyancy is removed, the microgravity flames have a wrinkle amplitude that is 2–3 times greater than 1-*g* flames. Flame stretch effects also are observed because the diffusionally unstable flames have larger wrinkle amplitudes than the stable cases. The particle imaging velocimetry velocity data show that two stabilizing mechanisms occur due to buoyancy: the conventional Rayleigh–Taylor mechanism and a baroclinic stabilization mechanism, which has not been observed previously in combustion processes. Measurements show that the flame generates new vorticity, and this flame-generated vorticity can help to suppress the flame wrinkling.

Nomenclature

A	= maximum amplitude of flame wrinkling
d	= vortex core diameter (0.8 cm)
Fr	= Froude number, $\rho_R U_\theta^2/(\Delta\rho g d)$
Fr^*	= Froude number based on flame speed; Eq. (1)
g	= gravitational acceleration
$S_{L,0}$	= unstretched laminar flame speed
T_R, T_P	= temperature of reactants, products
Γ	= circulation of flame-generated vorticity
$\Delta\rho$	= $\rho_R - \rho_P$
δ	= flame thickness
ρ_R, ρ_P	= density of reactants, products
τ	= $T_P/T_R - 1$
∇p_s	= hydrostatic pressure gradient
$\nabla\rho$	= density gradient of flame

Introduction

SEVERAL experiments have shown that buoyancy forces can significantly suppress the wrinkling of the reaction zone surface within a turbulent premixed flame; in addition, buoyancy alters the reaction zone surface area and the turbulent burning velocities. Bedat and Cheng,[1] Kostiuk and Cheng,[2] Durox et al.[3] and Durox[4] operated turbulent bunsen flames and V-flames in microgravity and found that flame properties differed dramatically from those measured at 1 *g*. Therefore, it is important to measure the relevant Froude numbers below which physical processes associated with buoyancy (such as the Rayleigh–Taylor and baroclinic torque mechanisms described subsequently) are comparable to other mechanisms, such as hydrodynamic and thermodiffusive instabilities.

In the present study it was decided to create an axisymmetric wrinkle in a flame surface using a repeatable and controllable disturbance, i.e., passing a vortex through the flame, and then measure the wrinkle amplitude with and without buoyancy forces present. A laminar flat premixed flame was interacted with a laminar toroidal vortex having a core diameter d and a variable rotational velocity U_θ. The relevant Froude number $\rho_R U_\theta^2/(\Delta\rho g d)$ was varied from 0.2 to 15.6 under 1-*g* conditions, and for the microgravity tests the Froude number is essentially infinite. In addition to quantifying the effects of buoyancy, the measurements create a database of buoyancy-free information about the canonical flame–vortex interaction problem. This flame–vortex problem provides a useful way to assess direct numerical simulation (DNS) schemes before attempting simulations of turbulent flames. The present microgravity data are being compared to the DNS simulations of Patnaik and Kailasanath[5] for the same flame–vortex operating parameters.

Rayleigh–Taylor and the Baroclinic Torque Mechanisms

The conventional Rayleigh–Taylor mechanism is one way in which wrinkles in a flame surface can be suppressed by buoyancy.[6–8] Figure 1 shows a wrinkle in a flame for which the dense reactants are below the lighter products, which is analogous to a wave on a water surface. Because of the Rayleigh–Taylor mechanism, buoyancy forces tend to reduce the wrinkle amplitude and, thus, create a flat surface between the two fluids. The physical process can be understood if one first considers a different situation for which a spherical pocket of reactants of volume V is surrounded by reactants at the same density ρ_R. There is no net force on this pocket of fluid because the downward gravitational force $\rho_R g V$ is balanced by an upward hydrostatic pressure force; the pressure is larger on the bottom of the pocket of fluid than on the top because pressure increases linearly with the depth of the fluid. If one now considers a second case in which a spherical pocket of dense fluid (reactants) of density ρ_R is surrounded by less dense fluid (products) of density ρ_P, of course this pocket of reactants falls downward because the hydrostatic pressure gradient in the less dense surrounding fluid, $\rho_P g$, is smaller than the pressure gradient in the first case, $\rho_R g$, and so the forces are not balanced. The wrinkle shown in Fig. 1 represents a situation that is intermediate to the two cases just considered. The volume of gas within the wrinkle in Fig. 1 has density ρ_R and is surrounded by gas of lower density ρ_P on the top side; it is surrounded by gas of density ρ_R on the bottom side. Thus, the pressure gradient on the top side of the wrinkle is less than on the bottom side. Thus, this volume of gas in the wrinkle falls downward, but not as fast as the spherical pocket described in the second case.

Pelce and Clavin[8] have calculated the ratio of this Rayleigh–Taylor stabilizing force to the inherent destabilizing force on a

Received July 9, 1997; revision received April 11, 1998; accepted for publication May 3, 1998. Copyright © 1998 by the American Institute of Aeronautics and Astronautics, Inc. All rights reserved.

*Ph.D. Candidate, Department of Aerospace Engineering. Member AIAA.

†Research Assistant, Department of Aerospace Engineering; currently Research Scientist, Combustion Research Facility, Sandia National Laboratories, Livermore, CA 94551. Member AIAA.

‡Research Assistant, Department of Aerospace Engineering; currently Technical Representative, International Launch Services, Lockheed Martin Corp., San Diego, CA 92101. Member AIAA.

§Professor, Department of Aerospace Engineering. E-mail: jamesfd@engin.umich.edu. Associate Fellow AIAA.

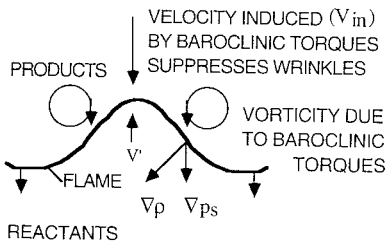

Fig. 1 Schematic of the baroclinic torques mechanism.

wrinkled flame that is due to the Landau hydrodynamic instability. They show that the ratio of the destabilizing (hydrodynamic) to stabilizing (Rayleigh–Taylor) forces scales with the Froude number based on flame properties, Fr^*, which is

$$Fr^* = (\rho_R/\rho_P)\left(S_{L,0}^2\right)/(gd) \tag{1}$$

The wrinkle diameter is d, and $S_{L,0}$ is the laminar burning velocity. Pelce and Clavin[8] also show that, when a critical Froude number is exceeded, the stabilizing buoyancy forces can no longer suppress the inherent hydrodynamic instability of the flame surface. Their analysis predicts a value for the critical Froude number associated with the Rayleigh–Taylor mechanism for a given Markstein length and a given density ratio (ρ_P/ρ_R).

The baroclinic torque mechanism represents a stabilizing process that differs from the Rayleigh–Taylor mechanism, yet it also is associated with buoyancy forces. The baroclinic torque mechanism is described by Drazen and Reid[7] and is known to damp out wrinkles in the interface between hot and cold gases in the atmosphere. In analyzing the present data it was realized that the baroclinic torque mechanism also can occur in combustion processes, as evidenced by the measurements to be described. The physical process is shown in Fig. 1. When pressure gradients and density gradients are not aligned, baroclinic torques create new vorticity, which creates new fluid motions, which can either suppress or amplify the flame wrinkles; this mechanism is fundamentally different from the Rayleigh–Taylor mechanism. In Fig. 1 the hydrostatic pressure force creates a pressure gradient vector ∇p_s that points downward. Within the flame, the density gradient vector $\nabla\rho$ is normal to the wrinkled flame surface. The vorticity transport equation is derived from the exact Navier–Stokes equations, and it states that the rate of change of the vorticity ω of each fluid element is

$$\frac{D\boldsymbol{\omega}}{Dt} = \frac{\nabla\rho\times\nabla p}{\rho^2} - \boldsymbol{\omega}\nabla\cdot\boldsymbol{v} + \boldsymbol{\omega}\cdot\nabla\boldsymbol{v} + \nu\nabla^2\boldsymbol{\omega} \tag{2}$$

The baroclinic torque term $(\nabla\rho\times\nabla p)/\rho^2$ is the only possible source of additional new vorticity that could be created at the flame interface shown in Fig. 1. The $-\omega\nabla\cdot v$ term represents attenuation (due to gas expansion) of any vorticity that already may be present in the reactants, so that it represents a net loss and not a source of new vorticity. The vortex stretching term $\boldsymbol{\omega}\cdot\nabla\boldsymbol{v}$ is zero because the wrinkle shown in Fig. 1 and the wrinkle used in the present experiment are axisymmetric. The diffusion term $\nu\nabla^2\omega$ causes a spreading of the vorticity in space and a reduction of the local vorticity but does not change the total vorticity that is averaged over all space.[9]

The new vorticity that is created at a rate equal to $(\nabla\boldsymbol{\rho}\times\nabla p_s)/\rho^2$ is a vector quantity that points out of the plane of the paper on the right-hand side of Fig. 1, as determined by the right-hand rule of vector cross products. Figure 1 shows the fluid motion in the products that is the result of the flame-generated vorticity associated with the baroclinic torque. The new vorticity induces a downward velocity near the centerline that is denoted V_{in}. This induced velocity counteracts the original upward motion in the disturbance and, therefore, attenuates the wrinkle in the flame surface. Thus, the baroclinic torque acts as a stabilizing mechanism in this case. It can be shown that for any disturbance shape, the baroclinic torque mechanism creates fluid motions that stabilize downward propagating flames and destabilize upward propagating flames. Prior to the present program,[10] there have been few measurements of vorticity near a flame, and so it was not known if the flame actually does generate vorticity in the manner that is predicted by Eq. (2). The measurements and analysis to follow indicate the Froude number at which the baroclinic mechanism becomes important.

Viscosity gradients in the flame also can create or destroy vorticity; three additional terms associated with viscosity gradients have been omitted from the right side of Eq. (2) because it is shown in the subsequent Discussion section that they contribute less than 4% of the vorticity change due to baroclinic or gas expansion mechanisms and, therefore, can be neglected. In a physical sense, the velocity of a fluid element will be slightly retarded as it crosses the thin flamefront if the average viscosity in the flamefront is increased; however, this viscosity effect is small because the element spends so little time in the flamefront.

Arrangement of Microgravity Drop Tower Experiment

Figure 2 shows the University of Michigan microgravity flame–vortex experiment that was operated in the NASA Lewis Research Center 2.2-s drop tower facility. The combustion chamber and the vortex that are shown in Fig. 3 are described in detail in Refs. 10–16. A rectangular chamber is filled with either a lean propane–air mixture at equivalenceratio of 0.58 or a lean methane–air mixture at equivalenceratio of 0.55. Two electrodes near the top of the chamber

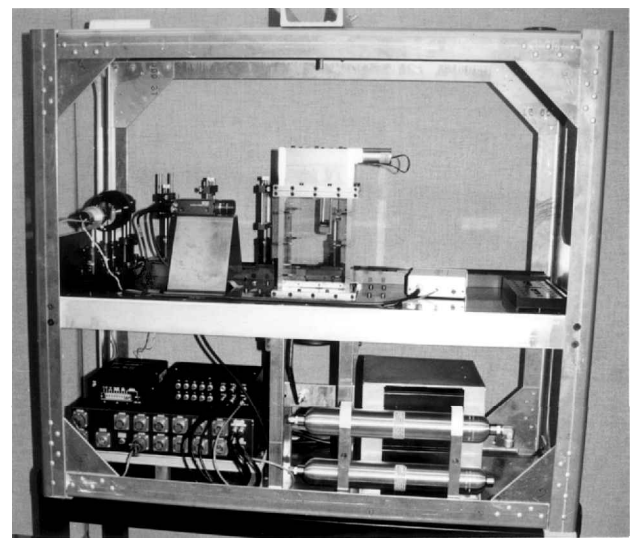

Fig. 2 University of Michigan microgravity flame–vortex interaction experiment. Top shelf, from left: pulsed xenon white light source, sheet forming optics, Sony charge-coupled device video camera, rectangular combustion chamber, video signal transmitter, 100-ft-long fiber optic cable. Lower shelf, from left: TT4A digital controller, power supply distribution electronics, spark electronics, xenon lamp power supply, fuel and air tanks, 24-V battery pack.

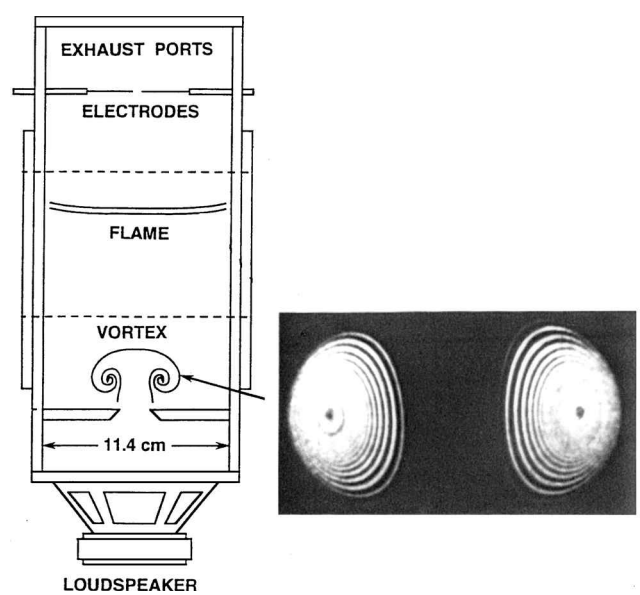

Fig. 3 Vortex used to create a repeatable disturbance in the flame surface. Laser light sheet image; oil droplets are added to vortex.

Table 1 Test conditions for the microgravity and 1-*g* studies

Condition	Wrinkled flame regime	Corrugated flames		Local extinction
Vortex strength $U_\theta/S_{L,0}$	1.3	2.1	3.6	10.0
Froude number $\rho_R U_\theta^2/(\Delta\rho g d)$	0.2	0.8	2.1	15.6
Methane,[a] microgravity	X[b]	X		
Methane, 1 *g*	**X**[c]	X	**X**	**X**
Propane,[d] microgravity	X	X		
Propane, 1 *g*	**X**	X	**X**	**X**

[a]Methane (lean) = thermodiffusively unstable.
[b]X = images of amplitude of flame wrinkling, no PIV data.
[c]**X** = images of amplitude of flame wrinkling and PIV data.
[d]Propane (lean) = thermodiffusively stable $S_{L,0} = 10$ cm/s, $d = 0.8$ cm.

are used to ignite the mixture on the centerline. The laminar flame kernel rapidly becomes a flat flame and propagates downward at a unstretched laminar burning velocity $S_{L,0}$ of 10 cm/s for either fuel. At the bottom of the chamber a loudspeaker is mounted 3 cm below a metal plate, which has a 2.0-cm-diam orifice. Pulsing the loudspeaker forces fluid through the orifice, creating a laminar toroidal vortex ring that moves upward and interacts with the flame. The radius of the vortex core is 0.4 cm, which is defined as the radial distance from the center of the vortex core to the location of maximum rotational velocity about the center of the core. The vortex strength is controlled by adjusting the maximum voltage applied to the loudspeaker; vortex strength is defined as the maximum rotational velocity (which occurs at the edge of the vortex core[14]; it varies from 7 to 100 cm/s. The fuel–air mixture inside the vortex is identical to that of the chamber into which the vortex moves.

Table 1 lists the conditions that were selected for the microgravity and the 1-*g* tests. Five vortex strengths were selected such that the values of the maximum rotational velocity at the edge of the vortex core, U_θ, normalized by $S_{L,0}$, are 1.3, 2.1, 3.6, and 10. The first value corresponds to the regime of wrinkled thin flames; the next two values correspond to the regime of corregated flames having pockets of unreacted gas; the largest vortex strength corresponds to local flame extinction. The values of the Froude number *Fr* are listed in Table 1; *Fr* is defined as $\rho_R U_\theta^2/(\Delta\rho g d)$. For all tests, $S_{L,0}$ is 10 cm/s, and the vortex core diameter d is 0.8 cm. All conditions could be imaged at 1 *g*, but not all conditions could be imaged in microgravity due to the diagnostic limitations.

The microgravity flame is visualized using two methods: For some runs the direct flame chemiluminescence is imaged, whereas for other runs oil drops are introduced and are illuminated by a white light sheet. The camera used is a Sony XC-75 video camera, which has 768 × 494 pixels, 3 lux sensitivity, and can be shuttered to 1/1000 s to help freeze the fluid motions. Each half-frame of the video cassette recorder output is digitized, and so images are collected at intervals of 1/60th of a second. The white light sheet is formed using a pulsed xenon arc lamp (EG&G Model FX-249/FYD-712 with PS-450 dc power supply) that provides 0.5 joule pulses at 60 pulses/s with a 10-μs pulse duration that is short enough to freeze the fluid motion. Each half-frame of the video camera is synchronized with the light source, so that images are obtained at a 60-Hz rate. The camera and xenon light source were sufficiently rugged to withstand numerous drops in the NASA Lewis Research Center drop tower.

The University of Michigan microgravity drop package is powered by a 28-V dc battery pack, which is connected to a power distribution box and dc converter to power the various electronic components, including the camera power supply, the xenon light source power supply, the spark electronics, the loudspeaker, the synchronization computer, and the solenoid valves. The synchronization computer is a Tattletale TT4A digital controller, which was programmed prior to each drop. Synchronization pulses were provided for the following events: the start of the drop, the opening of the exhaust ports, the pulsing of the xenon light source, the spark ignition, the pulsing of the loudspeaker, the closing of exhaust ports, and the shutdown of the light source and camera. To obtain proper synchronization, several calibration drops first were required for each condition because the speed of the flame in the laboratory coordinates in microgravity differed from that in 1 *g*; this

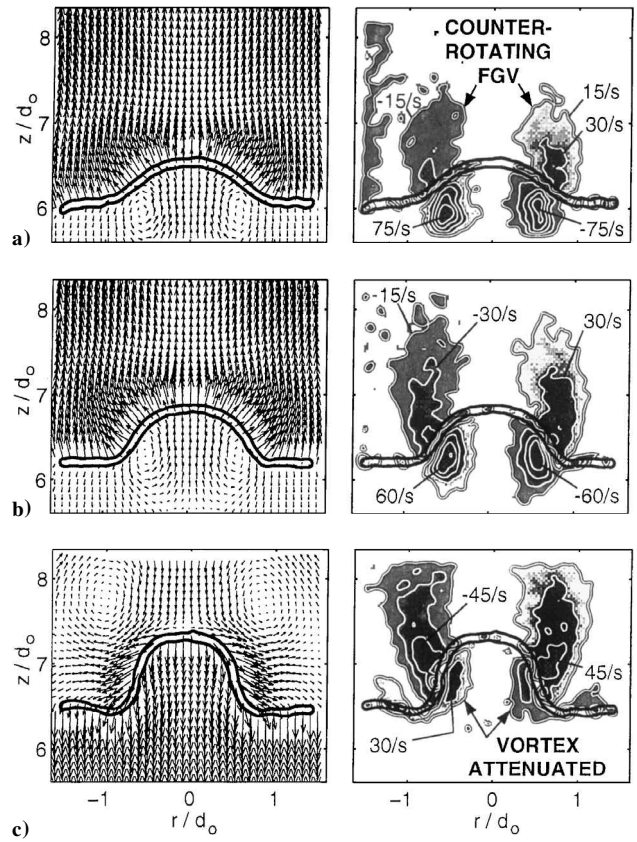

Fig. 4 PIV measurements of velocity (left) and vorticity contours (right) at 1 *g* that verify that vorticity is produced by the flame: a) and b) are in the frame of reference of the reactants, and c) is in the frame of reference of the products.

was attributed not to a change in the propagation speed $S_{L,0}$ but to a change in the upward exhaust velocity of the product gases.

Video images of the microgravity flames were digitized using a frame grabber board, and the gray scale of the black-and-white video images was converted to a color scale using Adobe Photoshop software. The particle imaging velocimetry (PIV) images of the 1-*g* flames were processed using techniques described in Refs. 10–13. In the PIV images, the upstream and downstream boundaries of the flame were determined by using the measured values of radial and axial velocity components u_r and u_z to determine div u at each grid location (every 0.5 mm). The flame boundary shown by the solid line in Fig. 4 is defined as the contour div $u = 0.5$ (div $u)_{\max}$ where (div $u)_{\max}$ is typically 400 s^{-1}. The initial vortex is seen in the reactants below the flame; the contours of flame-generated vorticity appear above the flame.

Results

Experimental Evidence of the Baroclinic Torque Mechanism

Prior to the microgravity drops, the 1-*g* experiment revealed evidence that the baroclinic torque mechanism occurs in combustion processes, which had not been realized previously. Figure 4 shows some measured velocity fields and vorticity fields for the case of a propane–air flame that is wrinkled by a vortex at 1 *g*. The solid lines shown represent the flame boundaries, as already defined. For clarity, only every ninth velocity vector is shown. Values of $U_\theta/S_{L,0}$ and Froude number are 1.3 and 0.2, respectively.

The flame wrinkle that is seen in Fig. 4 has the same shape as that in Fig. 1, and so baroclinic torques act in the manner described earlier. The data in Fig. 4 show that there is substantial flame-generated vorticity, as evidenced by the vorticity in the product gases (above the flame), which has a different sign of vorticity than that of the initial vortex, which is seen below the flame. The initial vortex moves upward and disappears at the flame front due to the large gas expansion term $(-\omega\nabla\cdot v)$ in the vorticity transport equation (1).

Baroclinic torques represent the only mechanism in the vorticity transport equation that could produce the flame-generated vorticity

that is seen in Fig. 4. Furthermore, this new vorticity is associated with buoyancy because the flame-generated vorticity is not observed if the buoyancy effects are decreased by increasing the Froude number above 2.1.

Effect of Buoyancy on Flame Wrinkling-Microgravity vs 1 *g*

The amplitude of the flame wrinkle was measured (as a function of time) for microgravity and for 1-*g* conditions for exactly the same forcing conditions, i.e., vortex strength. The differences between microgravity and 1-*g* results are attributed to buoyancy effects, which represent the sum of the effects associated with the Rayleigh–Taylor and baroclinic torque mechanisms. Estimates of the relative importance of the two buoyancy-related mechanisms are given in the next section. Several images of the flame–vortex interaction in microgravity are shown on the right-hand sides of Figs. 5–8. The left-hand side of each figure shows the corresponding 1-*g* flame. The 1-*g* run was performed within 20 min of the microgravity drop to ensure that all operating conditions were identical.

The primary conclusion that can be deduced from Figs. 5–8 is that the amplitude of the wrinkle in the flame is larger in microgravity than at 1-*g* for every case studied. Microgravity removes the two stabilizing mechanisms associated with buoyancy that were described earlier. In Fig. 5, for example, the lean methane–air flame at 1-*g* (on the left) is only wrinkled into a simple shape, whereas the microgravity flame (on the right) begins to roll up, forming a much

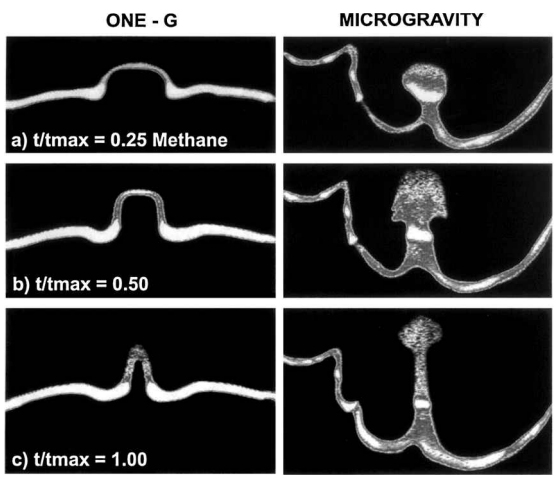

Fig. 5 Microgravity flames compared to 1-*g* flames: lean methane–air, vortex strength ($U_\theta/S_{L,0}$) 1.3; t_{max} is time of maximum amplitude of wrinkling; width of image 11.0 cm; vortex moves upward and flame propagates downward.

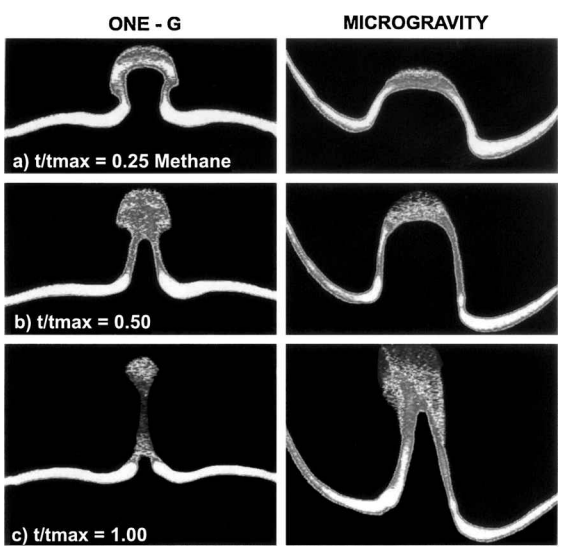

Fig. 6 Microgravity flames compared to 1-*g* flames: lean methane–air, vortex strength ($U_\theta/S_{L,0}$) 2.1.

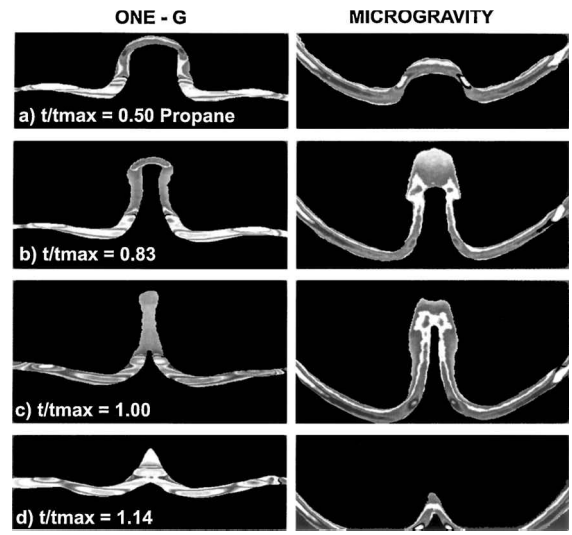

Fig. 7 Microgravity flames compared to 1-*g* flames: lean propane–air, vortex strength ($U_\theta/S_{L,0}$) 1.3.

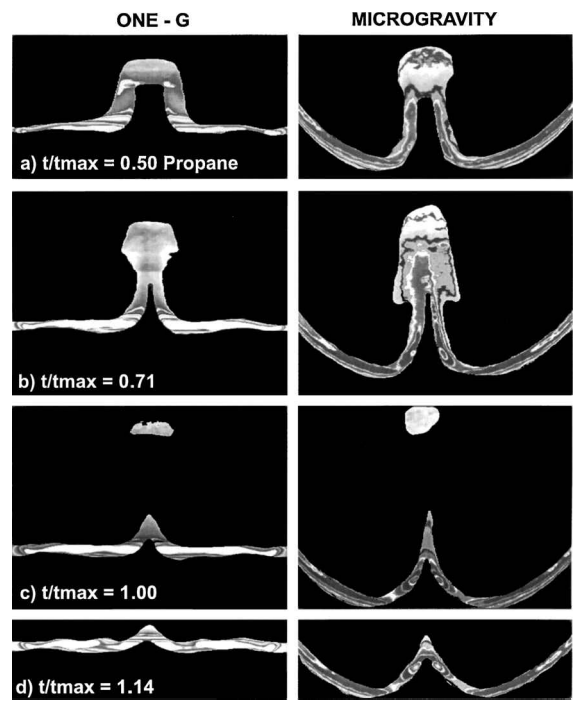

Fig. 8 Microgravity flames compared to 1-*g* flames: lean propane–air, vortex strength ($U_\theta/S_{L,0}$) 2.1; width of image 11.0 cm.

larger amplitude of the wrinkle and a thicker flame zone. Figure 6 shows that for a stronger vortex, the amplitude of the wrinkling increases, as expected, yet the microgravity flame always has a larger amplitude of wrinkling than the 1-*g* flame. The lean propane–air flames in Figs. 7 and 8 also show larger wrinkling in microgravity, and the rollup of the flame in the vortex is seen in the images on the right side of Figs. 7 and 8. Thus, as Figs. 5–8 show, microgravity flames undergo more wrinkling than 1-*g* flames.

A pocket of unburned reactants, which can be a source of unburned hydrocarbons and carbon monoxide, is observed in Fig. 8. The fundamental criterion governing whether the pocket of reactants will be consumed or not is as follows: The flame surrounding the pocket of reactants will be extinguished if the temperature decays sufficiently rapidly behind the flame due to radiative heat losses and if the pocket moves sufficiently rapidly so that it quickly enters the cooler products that are farther from the flame front. The present experiments have identified the history of the pockets that are formed by vortices,[14–16] and the computations of Patniak and Kailasanath[5] have considered cases for which the pockets are both consumed and not consumed.

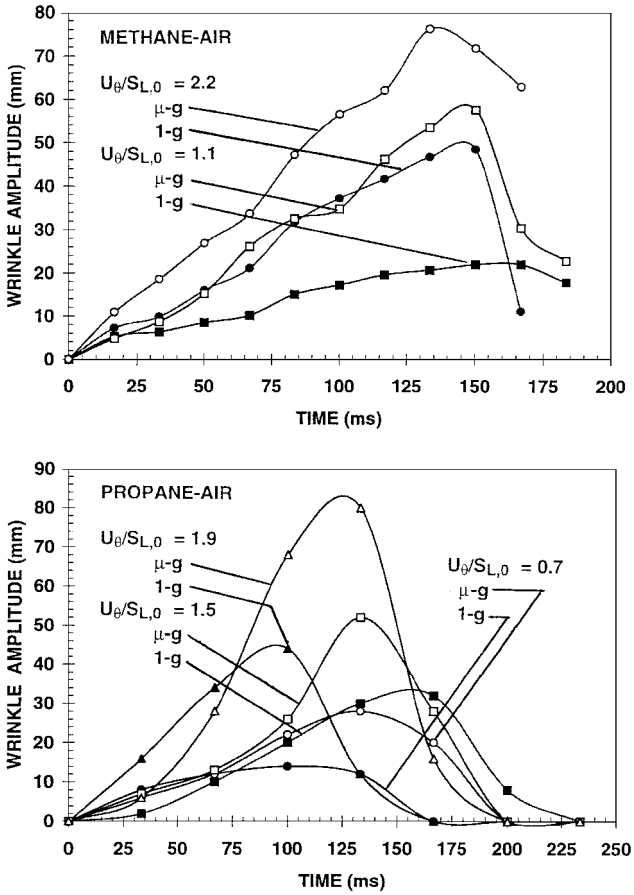

Fig. 9 Measured time history of the amplitude of flame wrinkling due to vortex passage in microgravity and at 1 *g*.

It is noted that the flame is extremely flat prior to the vortex interaction on the left-hand sides of Figs. 5–8, which corresponds to 1-*g* conditions with propane and methane fuel. These 1-*g* flames are seen to remain flat at locations far from the centerline. The microgravity flames, however, display some curvature prior to interaction in Figs. 5–8. The flame curvature is a small contribution to the overall strain rates (less than 5%), and it cannot be avoided in microgravity because there are no buoyancy forces to flatten the flame, and so the flame remains spherical. Flame curvature could be minimized if the flame is allowed to propagate for a longer time in a larger chamber, but this is not practical because hydrodynamic instabilities begin to wrinkle the flame after the interaction times chosen. The curvature of the present microgravity flames is sufficiently small such that the propagation speed and the wrinkling processes are not affected. The actual flame velocity in the laboratory coordinates is larger in the microgravity case because the products are not forced out of the chamber by buoyancy forces.

Figures 9 and 10 quantify the effects of buoyancy on flame wrinkling. The maximum amplitude of the flame wrinkle is plotted for various vortex strengths, fuel types, and gravitational accelerations. It is seen that flame wrinkling increases if the vortex strength is increased, as expected. For the methane–air cases, microgravity conditions cause the flame wrinkling to be two to three times that of the 1-*g* flames. For the propane–air cases, microgravity also causes a significant increase in flame wrinkling, which is 1.5–2 times that of the 1-*g* flames. The two fuel types yield somewhat different results because the propane–air flame is thermodiffusively stable and has a Markstein number of +8, whereas the methane–air flame is thermodiffusively unstable and has a Markstein number of −2, based on measurements of Tzeng et al.[17]

Discussion: Relative Importance of Baroclinic Torques

It is not possible to accurately measure the relative contributions from the four processes that affect flame wrinkling, namely, hydrodynamic, thermodiffusive, Rayleigh–Taylor, and baroclinic torque

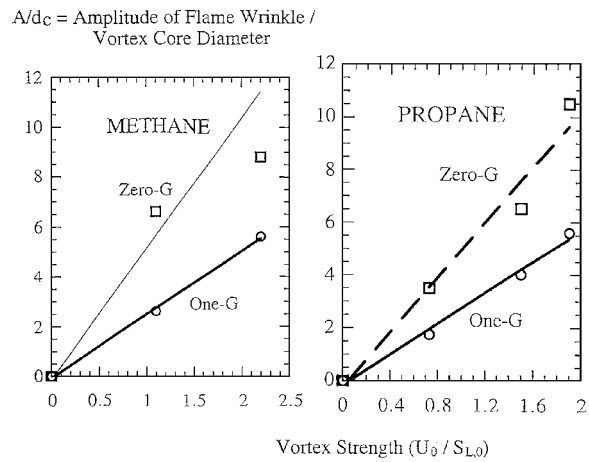

Fig. 10 Effect of buoyancy on the maximum amplitude of wrinkling of the lean methane–air and the lean propane–air flames.

mechanisms. However, a simple scaling analysis was performed to identify the parameter that determines the relative importance of the baroclinic torques, and some experimental values of this parameter are presented.

The magnitude of the baroclinic torque is given by the first term on the right-hand side of Eq. (2), which is $(\nabla\rho \times \nabla p)/\rho^2$. The density gradient, the hydrostatic pressure gradient, and the density difference across the flame scale as

$$\nabla\rho = \Delta\rho/\delta, \qquad \nabla p_s = \rho_R g, \qquad \Delta\rho = \tau\rho_P \tag{3}$$

where δ is the flame thickness and the heat release parameter τ is $\rho_R/\rho_P - 1$. The magnitude of the flame-generated vorticity is the product of the production rate and the time required by a fluid element to cross the flame, within which all vorticity production occurs. The flame transit time Δt scales as $\delta/S_{L,0}$, and so the flame-generated vorticity is

$$(\nabla\rho \times \nabla p)\rho^{-2}\Delta t = g/S_{L,0} \tag{4}$$

where the product of τ and (ρ_P/ρ_R) is nearly unity. The total circulation Γ associated with the preceding vorticity scales as the vorticity multiplied by πd^2, where the vortex core diameter d is proportional to the characteristic length of the wrinkle, so that

$$\Gamma = \pi g d^2 \big/ S_{L,0} \tag{5}$$

The induced velocity V_{in} on the centerline in Fig. 1 due to the flame generated vorticity is given by the law of Biot and Savart for a line vortex,

$$V_{\text{in}} = \Gamma/(\pi d) = gd/S_{L,0} \tag{6}$$

The dynamic force (per unit volume) associated with a fluid motion of velocity V_{in} is given by $[\rho_P V_{\text{in}}^2/d]$, which is an estimate of the convective term in the momentum equation. Thus, the force per unit volume due to the baroclinic torque is

$$\frac{\text{baroclinic force}}{\text{volume}} = \frac{\rho_P V_{\text{in}}^2}{d} = \frac{\rho_P (gd/S_{L,0})^2}{d} \tag{7}$$

The destabilizing force per unit volume associated with the hydrodynamic instability is shown by Pelce and Clavin[8] to scale with $[\rho_R S_{L,0}^2/d]$. Combining this with Eq. (7) yields a ratio of forces equal to

$$\frac{\text{baroclinic force/volume}}{\text{hydrodynamic force/volume}} = c_1 (Fr^*)^{-2} \tag{8}$$

where the constant c_1 is $(\rho_P/\rho_R)^3$ and the Froude number Fr^* that is associated with the flame velocity is given by Eq. (1). Previously,

Pelce and Clavin[8] have shown that the ratio of Rayleigh–Taylor to hydrodynamic forces scales as

$$\frac{\text{Rayleigh–Taylor force}}{\text{hydrodynamic force}} = (Fr^*)^{-1} \tag{9}$$

Equations (8) and (9) indicate that at large Froude numbers both the baroclinic and the Rayleigh–Taylor mechanisms disappear, as expected; at small Froude numbers both mechanisms should be important, but as the Froude number increases, the Rayleigh–Taylor mechanism should dominate over the baroclinic torque mechanism.

For the experimental conditions shown in Fig. 4, the measured value of Γ is approximately 200 cm^2/s and d is 0.8 cm, so that the induced velocity caused by baroclinic torques, V_{in} given by Eq. (6), is 32 cm/s. Thus, baroclinic torques induce a velocity that is three times the laminar burning velocity, which is 10 cm/s. Furthermore the induced velocity is larger than the maximum velocity in the disturbance, i.e., the vortex, itself, which is 14 cm/s. The Rayleigh–Taylor mechanism also creates a velocity that restores the disturbed surface to a level position, which is approximately the velocity that a falling bubble of diameter d would have in the presence of gravity. This velocity is $(2gd)^{1/2}$; d is 0.8 cm, so that the Rayleigh–Taylor induced velocity is approximately 39 cm/s. This value is nearly equal to the baroclinic-induced velocity of 32 cm/s. Thus, for the conditions of the present experiment, the Rayleigh–Taylor and the baroclinic torque stabilization mechanisms are of nearly equal strength.

It is now shown that viscosity gradients terms in the vorticity transport equation (2) contribute less than 4% of the vorticity change associated with baroclinic or gas expansion mechanisms and, therefore, can be neglected. Mueller[18] gives a complete derivation of the vorticity transport equation for a Newtonian fluid with variable density and viscosity; the three terms associated with viscosity that were not included on the right-hand side of Eq. (2) are

$$\nabla \times [(2/\rho)\nabla\mu \cdot \varepsilon] + \nabla\nu \times [\nabla^2 u + \nabla(\nabla \cdot u)] - [\nabla\rho \times \nabla(\lambda\nabla \cdot u)]/\rho^2$$

where ε is the strain rate tensor and μ and λ are the first and second coefficients of viscosity. To estimate the importance of these terms, consider the first term and set $\nabla\mu$ approximately equal to $(\mu_P - \mu_R)/\delta$, where the viscosity of the products is $(T_P/T_R)^{1/2}\mu_R$ and δ is the flame thickness. Thus, $\nabla\mu/\rho$ is $[(T_P/T_R)^{1/2} - 1]\nu_R/\delta$. Using Eq. (4), the ratio of viscous to baroclinic vorticity production rates is

$$\frac{\text{viscous generation}}{\text{baroclinic generation}} = \frac{2\left[(T_P/T_R)^{\frac{1}{2}} - 1\right]\left(\nu_R/\delta^2\right)\varepsilon}{g/\delta} \tag{10}$$

where Δt in Eq. (4) was replaced with $\delta/S_{L,0}$. The following values were measured for the present experiment: $T_P/T_R = 5$, $\nu_R = 0.15$ cm^2/s, and $\delta = 2$ mm; Ref. 12 shows that the measured strain rate ε is typically 20 s^{-1}. The resulting ratio shown in Eq. (10) has the value of 0.04; thus, viscous generation of vorticity can be neglected and less than a 4% error results.

Experimental uncertainties in the reported data can arise due to uncertainties in four quantities: the PIV velocity values, the vortex strength, the fuel–air equivalence ratio, and the digitized contour of the flame shape. The fuel–air equivalence ratio was set using choked orifices to monitor the fuel and airflow rates; the pressure gauges had an accuracy of $\pm 3\%$ and the flame speed was measured to be 10 ± 0.5 cm/s, and so the maximum difference in flame speeds from run to run was less than 10%. The vortex strength was determined by the voltage applied to the loudspeaker, which varied by less than 5% from run to run. The digitized contour of the flame shape was determined by scanning the video images and applying Adobe Photoshop software. Errors in determining the flame wrinkle amplitude from the digitized images were only those due to a small blurring of the flame boundary, and these errors are less than 5%.

The PIV velocity images that were obtained at 1 g displayed less than a 4% difference between adjacent velocity vectors in the product gases, which move upward in a laminar fashion at approximately 50 cm/s. Because the flow of product gases is laminar, this 4% random scatter can be attributed to experimental errors associated with the PIV system. The smooth variations in the velocity field in Fig. 4 and the symmetry of the images in Fig. 4 confirm that the PIV uncertainties are small. The laminar propane–air flame at 1 g is flat to within one flame thickness, as shown in Ref. 10; the flame must be given sufficient time to evolve from a kernel to a flat flame (aided by buoyancy), yet after too long a time, the flame wrinkles spontaneously as hydrodynamic instabilities intensify.

Conclusions

1) Microgravity studies in the NASA Lewis Research Center 2.2-s drop tower show that when the stabilizing influence of buoyancy is removed, the wrinkling of a premixed flame caused by a repeatable vortex disturbance increases by as much as a factor of three.

2) The degree of wrinkling of a methane–air flame is larger than that of a propane–air flame, for both microgravity and 1-g conditions, because the methane–air flames are thermodiffusively unstable.

3) PIV images of the vorticity field at 1 g indicate that baroclinic torques due to buoyancy create flame-generated vorticity, which induces a velocity that suppresses flame wrinkles. The baroclinic mechanism that is identified in the present study can be an important stabilizing mechanism at low Froude numbers.

4) Scaling concepts indicate that the baroclinic torque mechanism scales with Froude number in a manner that differs from that of the Rayleigh–Taylor mechanism; the ratio of baroclinic torques to the Rayleigh–Taylor stabilizing forces scales inversely with Froude number. For the present experiment, the velocity induced by baroclinic torques is about equal to that induced by the Rayleigh–Taylor mechanism, so that baroclinic torques are important but not dominant.

5) The use of a toroidal vortex is shown to be a useful way to perturb a flame in a controllable, repeatable manner while retaining much of the physics associated with turbulent flames.

Acknowledgments

This microgravity science study was supported by NASA Grant NAG 3-1639, which was monitored by J. Brooker of NASA Lewis Research Center. The 1-g work was supported by National Science Foundation Grants CTS-912 3834 and CTS 952 9203, which were administered by M. Linevsky and Farley Fisher. The authors thank David Reuss, M. C. Drake, and M. Rosalik of General Motors Research and Development for their collaborative efforts in Refs. 10, 12, 13, 15, and 16, which provide comparisons to the present results.

References

[1] Bedat, B., and Cheng, R. K., "Effects of Buoyancy on Premixed Flame Stability," *Combustion and Flame*, Vol. 107, No. 1, 1996, pp. 13–23.

[2] Kostiuk, L. W., and Cheng, R. K., "The Coupling of Conical Wrinkled Flames with Gravity," *Combustion and Flame*, Vol. 103, No. 1, 1995, pp. 27–40.

[3] Durox, D., Baillot, B., Scoufflaire, P., and Prud'homme, R., "Some Effects of Gravity on the Behavior of Premixed Flames," *Combustion and Flame*, Vol. 82, No. 1, 1990, pp. 66–74.

[4] Durox, D., "Effects of Gravity on Polyhedrial Flames," *Twenty-Fourth Symposium (International) on Combustion*, Combustion Inst., Pittsburgh, PA, 1992, pp. 197–204.

[5] Patniak, G., and Kailasanath, K., "A Computational Study of Local Quenching in Flame–Vortex Interactions with Radiative Losses," *Twenty-Seventh Symposium (International) on Combustion*, Combustion Inst., Pittsburgh, PA (to be published).

[6] Chandrasekar, S., *Hydrodynamic and Hydromagnetic Instabilities*, Oxford Univ. Press, London, 1961.

[7] Drazen, P. G., and Reid, W. H., *Hydrodynamic Stability*, Cambridge Univ. Press, London, 1981.

[8] Pelce, P., and Clavin, P., "Influence of Hydrodynamics and Diffusion upon the Stability Limits of Laminar Premixed Flames," *Journal of Fluid Mechanics*, Vol. 124, Nov. 1982, pp. 219–237.

[9] Ashurst, W. T., and McMurtry, P. A., "Flame Generation of Turbulence: Vortex Dipoles from Monopoles," *Combustion Science and Technology*, Vol. 66, Nos. 1, 2, 1989, pp. 17–37.

[10] Mueller, C. J., Driscoll, J. F., Reuss, D., Drake, M., and Rosalik, M., "Vorticity Generation and Attenuation as Vortices Convect Through a Premixed Flames," *Combustion and Flame*, Vol. 112, No. 2, 1998, pp. 342–358.

[11] Driscoll, J. F., Sutkus, D., Roberts, W., Post, M., and Goss, L., "The Strain Exerted by a Vortex on a Flame—Determined from Velocity Field Images," *Combustion Science and Technology*, Vol. 96, Nos. 3, 4, 1994, pp. 213–229.

[12]Mueller, C., Driscoll, J. F., Reuss, D., and Drake, M., "Effect of Unsteady Stretch on the Strength of a Freely Propagating Flame Wrinkled by a Vortex," *Twenty-Sixth Symposium (International) on Combustion*, Combustion Inst., Pittsburgh, PA, 1996, pp. 347–353.

[13]Mueller, C., Driscoll, J. F., Roberts, W. L., Drake, M. C., and Smooke, M. D., "Effect of Stretch Rate on Flame Chemistry During a Transient Flame–Vortex Interaction—To Assess Flamelet Models," *Combustion and Flame*, Vol. 100, No. 2, 1995, pp. 323–331.

[14]Roberts, W., and Driscoll, J. F., "A Laminar Vortex Interacting with a Premixed Flame: Formation of Pockets of Reactants," *Combustion and Flame*, Vol. 87, No. 2, 1991, pp. 245–256.

[15]Roberts, W. L, Driscoll, J. F., Drake, M. C., and Ratcliffe, J., "OH Fluorescence Images of the Quenching of a Premixed Flame by a Vortex," *Twenty-Fourth Symposium (International) on Combustion*, Combustion Inst., Pittsburgh, PA, 1992, pp. 169–176.

[16]Roberts, W. L., Driscoll, J. F., Drake, M. C., and Goss, L. P., "Images of the Quenching of a Flame by a Vortex—To Quantify Regimes of Turbulent Combustion," *Combustion and Flame*, Vol. 94, No. 1, 1993, pp. 58–69.

[17]Tzeng, L.-K., Ismail, M. A., and Faeth, G. M., "Laminar Burning Velocities and Markstein Numbers of Hydrocarbon/Air Flames," *Combustion and Flame*, Vol. 95, No. 3, 1993, pp. 410–426.

[18]Mueller, C. J., "Measurements of Flame–Vortex Interaction Dynamics and Chemistry," Ph.D. Thesis, Dept. of Aerospace Engineering, Univ. of Michigan, Ann Arbor, MI, Sept. 1996.

K. Kailasanath
Associate Editor